

Alma Mater Studiorum Università di Bologna  
Archivio istituzionale della ricerca

Performance analysis of CO<sub>2</sub> thermal management system for electric vehicles in winter

This is the final peer-reviewed author's accepted manuscript (postprint) of the following publication:

*Published Version:*

Wang, H., Song, Y., Valdiserri, P., Rossi di Schio, E., Yang, X., Wang, X., et al. (2024). Performance analysis of CO<sub>2</sub> thermal management system for electric vehicles in winter. *APPLIED THERMAL ENGINEERING*, 236, 1-12 [10.1016/j.applthermaleng.2023.121700].

*Availability:*

This version is available at: <https://hdl.handle.net/11585/946115> since: 2023-10-24

*Published:*

DOI: <http://doi.org/10.1016/j.applthermaleng.2023.121700>

*Terms of use:*

Some rights reserved. The terms and conditions for the reuse of this version of the manuscript are specified in the publishing policy. For all terms of use and more information see the publisher's website.

This item was downloaded from IRIS Università di Bologna (<https://cris.unibo.it/>).  
When citing, please refer to the published version.

(Article begins on next page)

## Performance analysis of CO<sub>2</sub> thermal management system for electric vehicles in winter

Haidan Wang<sup>a,b</sup>, Yulong Song<sup>a</sup>, Paolo Valdiserri<sup>b</sup>, Eugenia Rossi di Schio<sup>b</sup>, Xu Yang<sup>a\*</sup>, Xixi Wang<sup>c</sup>  
Feng Cao<sup>a\*</sup>

<sup>a</sup>School of Energy and Power Engineering, Xi'an Jiaotong University, Xi'an 710049, China

<sup>b</sup>Department of Industrial Engineering, University of Bologna, Bologna, Italy

<sup>c</sup>Yutong Bus Co., Ltd., Zhengzhou, China

\*Corresponding author, Email: fcao@mail.xjtu.edu.cn (Feng Cao); yangzx@mail.xjtu.edu.cn (Xu Yang);

Tel: 86-029-82663583;

Fax: 86-029-82663583

### Abstract

CO<sub>2</sub> is well-suited for thermal management systems (TMSs) in electric vehicles, particularly in winter when both the cabin air and the battery require heating. However, due to the distinct heat exchange boundary conditions of these two heated components, traditional theories of optimal operation of CO<sub>2</sub> cycle are not applicable. In this paper, the system characteristics of a CO<sub>2</sub> TMS in the cabin-and-battery mixed heating mode are comprehensively investigated. The results show that there is a pseudo-optimal discharge pressure that maximizes the COP<sub>TMS</sub>, regardless of whether the system is operating in a transcritical or subcritical mode. In addition, besides the global optimal COP<sub>TMS</sub>, there may still be other local maximum points, which are determined by the CO<sub>2</sub> flow distribution in both gas coolers and the COP rise rate of the battery cycle. Furthermore, this work offers a thorough investigation of the impact of essential factors on the pseudo-optimal discharge pressure and proposes an accurate prediction approach for the best control of the CO<sub>2</sub> TMS. The CO<sub>2</sub> TMS can still ensure a COP<sub>TMS</sub> above 2.0 to meet the thermal demands of both the cabin and the battery even under the challenging operating circumstances of -20 °C, proving the technology's great

1 competitiveness.

2

3 **Keywords**

4 Transcritical CO<sub>2</sub> system, Heat pump technology, Thermal management system,

5 Optimal performance, Electric vehicles.

6

<b>Nomenclature</b>			
A	Area, (m <sup>2</sup> )	TMS	Thermal management system
$C_d$	discharge coefficient		
$c_p$	Specific heat capacity, (kJ/(kg·K))	<b>Greek symbols</b>	
h	Enthalpy, (kJ/kg)	$\alpha$	Heat transfer coefficient, (W/(m <sup>2</sup> ·K))
$L_{vap}$	latent vaporization heat of water, (kJ/kg)	$\varepsilon$	Pressure ratio of compressor
$\dot{m}_{cond}$	condensate mass flow rate, (kg/s)	$\eta_e$	Compressor motor efficiency
$\dot{m}_{CO_2}$	mass flow rate of CO <sub>2</sub> , (kg/s)	$\eta_{is}$	Compressor isentropic efficiency
N	The number of segments of heat exchanger	$\eta_V$	The ratio of the theoretical volume of the expander to the compressor
$\dot{N}_{com}$	Speed of compressor, (RPM)	$\rho$	Density, (kg/m <sup>3</sup> )
P	Pressure, (bar)		
$\dot{Q}$	Heat flow, (W)	<b>Subscripts</b>	
T	Temperature, (°C)	a	Ambient
$\dot{V}$	Coolant flow rates, (L/min)	air	Air
$V_d$	Displacement, (m <sup>3</sup> )	bat	Battery heating cycle
$\dot{W}$	Power consumption, (W)	cab	Cabin air heating cycle
		c	Coolant
<b>abbreviations</b>		com	Compressor
AC	Air conditioning	dis	Discharge of Compressor
BTMS	Battery thermal management system	EEV	Electronic expansion valve
COP	Coefficient of performance	j	Index of each segment
EEV	Electronic expansion valve	in	Inlet
EV	Electric vehicle	opt	Optimal
HP	Heat pump	out	Outlet
HX	Heat exchanger	pse-opt	Pseudo-optimal
HVAC	Heating, ventilation and air	suc	Suction of the compressor

	conditioning		
IHX	Internal heat exchanger	TMS	Thermal management system
PTC	Positive temperature coefficient	wall	Tube wall of heat exchangers

1

## 2 **1 Introduction**

3 Traditional internal combustion engine vehicles are gradually being replaced with  
4 electric vehicles (EVs) as a result of the global energy crisis and air pollution [1].  
5 Rechargeable lithium-ion batteries have become the primary source of power for EVs  
6 due to their high specific power, long cycle life, and high specific energy density [2].  
7 With an ideal operating temperature range of 10 °C to 50 °C, lithium-ion batteries are  
8 quite sensitive to ambient temperature [3]. The temperature differential between the  
9 cell should be smaller than 5 °C to increase service life [4]. At low temperatures,  
10 lithium-ion batteries lose a significant amount of their capacity and power density. In  
11 recent years, as batteries' size and capacity have increased, air-cooled battery thermal  
12 management systems (BTMS) have hardly been able to keep up [5]. Liquid cooling,  
13 however, can improve battery performance at high rate of charge and discharge [6].  
14 The liquid cooling BTMS can be more suitable for EVs.

15 In order to keep the passengers comfortable, the cabin air must be either cooled  
16 or heated in addition to meeting the needs of the battery [8]. Since there is no internal  
17 combustion engine in EVs that can generate enough waste heat [9], and the use of a  
18 positive temperature coefficient heater can significantly compromise the cruising range  
19 [10], the integrated air conditioning (AC)/ heat pump (HP) system is an energy-saving  
20 way to meet passengers comfort requirements [11-13]. In addition, the heating and  
21 cooling needs of the battery can be met by using the integrated AC/HP system by  
22 adding heat exchangers and parallel valves [14-15].

23 Park et al. [16] created a numerical model of refrigerant-based BTMS. The  
24 findings indicated that refrigerant temperature was more closely connected to battery  
25 temperature than refrigerant mass flow rate. According to Cen and Jiang [17], an EV  
26 battery pack's thermal performance can be significantly improved by a battery cooling

1 system that is connected to the main AC system via an additional expansion valve.  
2 Comprehensive research was done on the BTMS performance by Tang et al. [18]. The  
3 findings revealed that if the compressor speed is greater than 4000 rpm, the battery  
4 inlet coolant temperature can remain below 25 °C even when the surrounding  
5 temperature is above 40 °C. Shen and Gao [19] created a simulation model for the  
6 refrigerant-based BTMS and discovered that it can effectively reduce the battery  
7 temperature rise ( $\approx 25$  °C). Even in high-temperature and high-speed settings, it is  
8 possible to guarantee the temperature consistency across battery cells to within 3 °C.  
9 Tian et al. [20] proposed TMS for battery cooling, motor cooling, and cabin thermal  
10 comfort. With motor waste heat recovery, the coefficient of performance (COP) was  
11 raised to 25.55%. TMS heaters increased a vehicle's operating range by 31.71% when  
12 compared to PTC heaters. A TMS based on refrigerants was proposed by Guo and Jiang  
13 [21]. They showed that the suggested TMS, which has both a cabin-and-battery mixed  
14 cooling mode as well as a cabin-and-battery mixed heating mode, can successfully  
15 control both the cabin's air temperature and the battery pack's temperature.

16 It is worth noting that the above studies all use R134a as the refrigerant, which  
17 has a GWP of 1430 and is about to be replaced [22]. Carbon dioxide, as an  
18 environmentally friendly refrigerant, has now received attention in the field of  
19 automotive air conditioning. In particular, the excellent heating performance of CO<sub>2</sub>  
20 systems in winter has the potential to solve the problem of mileage anxiety caused by  
21 winter heating [23-25]. In addition, when the outlet temperature of the gas cooler is  
22 higher than 30 °C, there is an optimal discharge pressure in the supercritical zone due  
23 to the gradient properties of the isotherms to maximize the COP [26]. However, Wang  
24 et al. [27] demonstrated that there exists an optimal discharge pressure to be controlled  
25 in subcritical conditions due to the heat transfer capacity limitation of the gas cooler in  
26 winter conditions. This particular optimal discharge pressure is denoted as the pseudo-  
27 optimal discharge pressure ( $P_{\text{pes-opt}}$ ).

28 Yin et al. [28] proposed a novel CO<sub>2</sub> system with battery evaporative cooling to  
29 deal with the potential thermal runaway problem due to the control instabilities of two-

1 phase evaporative cooling. The cooling characteristics of a transcritical CO<sub>2</sub> TMS were  
2 studied by Wang et al. [29] They revealed the effects of CO<sub>2</sub> evaporation temperature  
3 and vapor quality on stable optimal discharge pressure control.

4 Although plentiful excellent researches have been carried out, more research is  
5 still needed on the CO<sub>2</sub> thermal management systems used in EVs, particularly in  
6 winter heat pump conditions where both the battery and cabin must be heated  
7 simultaneously. In this paper, a liquid-cooled CO<sub>2</sub> thermal management system test rig  
8 and simulation models were analyzed to close the research gap. Additionally, numerous  
9 PI controllers and a cabin thermal model were combined to fully analyze the winter  
10 performance of the CO<sub>2</sub> liquid-cooled thermal management system. Furthermore, we  
11 demonstrate that there exists a global pseudo-optimal discharge pressure in the cabin-  
12 and-battery mixed heating mode regardless of the system state of subcritical or  
13 transcritical cycles. In addition to the global optimal value, other local maximum points  
14 may still exist. To accurately predict the optimal performance to be attained by the  
15 TMS, it is then investigated how variable parameters such as ambient temperature,  
16 battery thermal demand (including chiller inlet coolant temperature and coolant flow  
17 rate), and passenger compartment fresh air ratio (i.e., HVAC inlet air temperature)  
18 affect the  $P_{\text{pes-opt}}$  value. Finally, a  $P_{\text{pse-opt}}$  prediction equation is proposed for maximizing  
19 the performance of CO<sub>2</sub> thermal management system in cabin-and-battery mixed  
20 heating mode for winter. It presents a solution for the optimal control of the CO<sub>2</sub>  
21 thermal management system. Maximum energy efficiency could be achieved with this  
22 research, which will also increase the driving range of EVs.

## 24 **2 System description and modeling details**

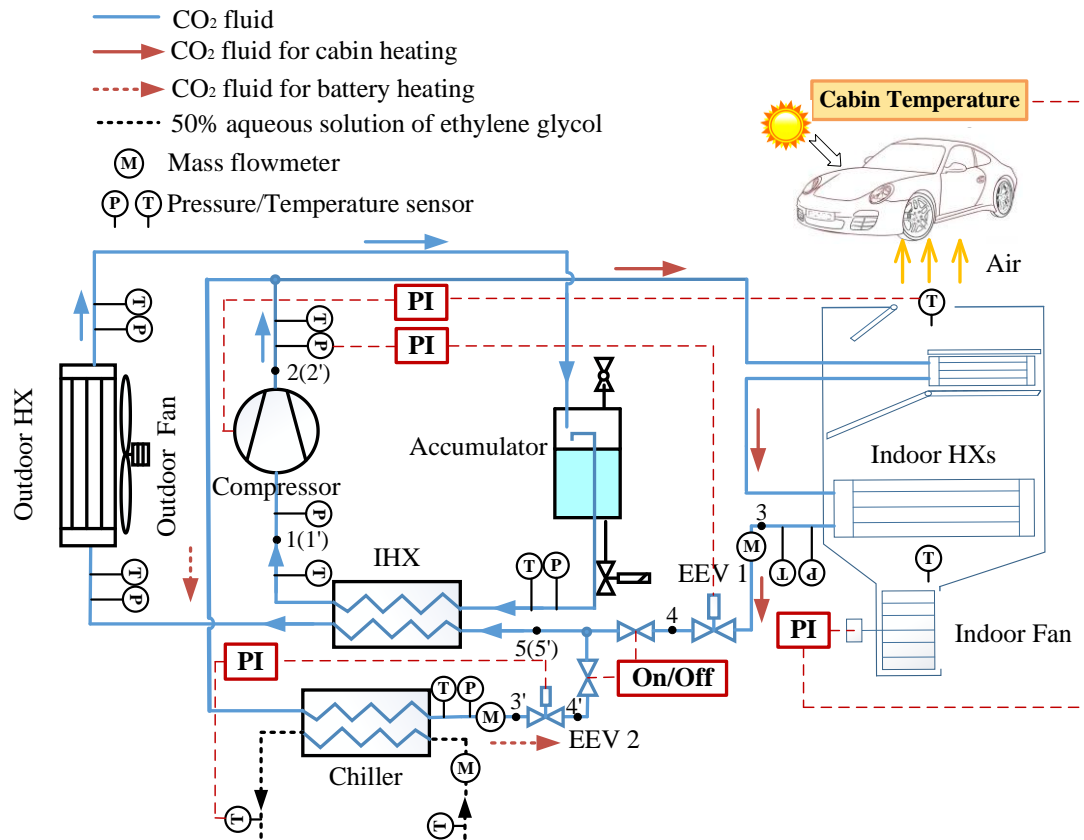
### 25 **2.1 System description**

26 Fig. 1. displays the schematic diagram of the CO<sub>2</sub> thermal management system  
27 that can jointly heat the cabin air and the battery. The compressor compresses the CO<sub>2</sub>  
28 fluid into a high-temperature, high-pressure superheated vapor, which is then split into  
29 two streams. One path goes via the electronic expansion valve (EEV) 1 to become a

1 low-temperature, low-pressure fluid after flowing into the indoor heat exchanger (HX)  
2 to warm the cabin. The other path enters the chiller where the battery is heated (A 50%  
3 aqueous solution of ethylene glycol is used to heat the battery after absorbing heat in  
4 the chiller). The CO<sub>2</sub> fluid changes into a low-temperature, low-pressure fluid as it  
5 passes through the EEV 2. The combined fluid from the two paths passes through the  
6 internal heat exchanger (IHX) before entering the outdoor HX for evaporation.  
7 Saturated vapor from the accumulator travels back to the compressor through the IHX.  
8 In this mode, the IHX does not work because it performs the heat exchange of the low-  
9 pressure two-phase fluid and the saturated vapor. IHX performs effectively only in  
10 the cooling mode [12]. Fig.2. shows the lgP-h diagram of the system. In addition, 4 PI  
11 controllers are designed to ensure the smooth operation of the system:

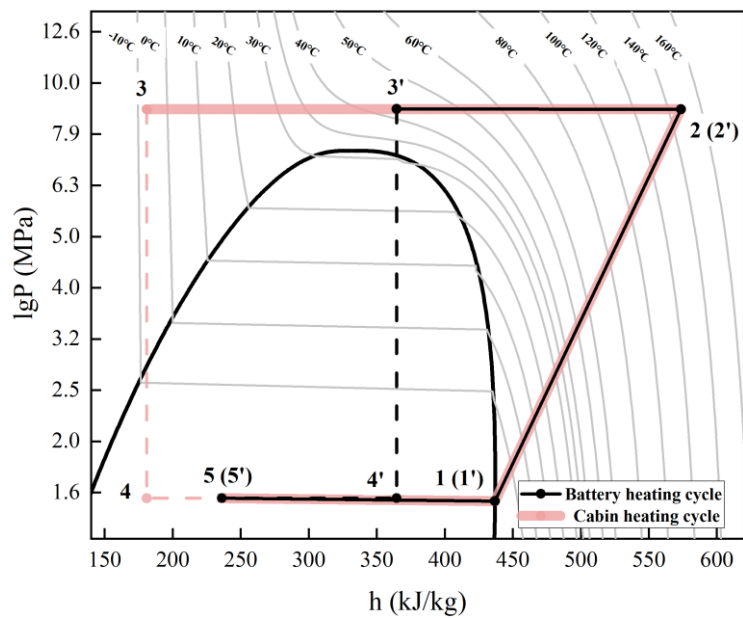
- 12 1) The temperature of the air sent into the cabin was set at 42 °C by adjusting the speed  
13 of the compressor;
- 14 2) The temperature of the cabin air was set at 20 °C by adjusting the speed of the  
15 indoor fan;
- 16 3) The discharge pressure of the compressor was adjusted by adjusting the flow area  
17 of EEV 1;
- 18 4) A 2 °C coolant temperature gradient between the inlet and outlet of the chiller was  
19 achieved by adjusting the EEV 2, ensuring uniform battery cell temperature.

20



1  
2  
3

Fig.1. The schematic diagram of the CO<sub>2</sub> TMS.



4  
5  
6

Fig.2. The lgP-h diagram of the heating cycle.

7 **2.2 modeling details**



1 In this study, the GT-SUITE is used as a platform to build a complete CO<sub>2</sub> thermal  
2 management system according to a rationally designed experimental rig. A cabin model  
3 as well as PI controllers were added to investigate the performance of the TMS in  
4 winter. GT-SUITE is a comprehensive system simulation software that encompasses  
5 multiple physical domains involving 1D and 3D simulations. It covers various physical  
6 fields such as fluid dynamics, heat transfer, mechanics, electrochemistry, and more.  
7 GT-SUITE is widely used for simulation work in thermodynamics-related domains  
8 [30-32] and vehicles [33].

9

### 10 **2.2.1 Heat exchanger models**

11 All heat exchangers are based on the *HxMaster* and *HxSlave* models. The  
12 *HxMaster* template is used to model heat transfer between the fluid on one side of a  
13 heat exchanger and the wall of the heat exchanger. Most characteristics of the heat  
14 exchanger (the detailed structure, materials, weight, and heat transfer correlations of  
15 the heat exchanger et.al) are entered in the *HxMaster* template, and the slave part is  
16 generally only of interest to declare initial conditions. The heat exchanger models are  
17 constructed using the moving boundary method.

18

19 Table 1

20 The modeling specifics of components.

---

Equipment	Specification
-----------	---------------

---

---

	Type: microchannel finned tube	
	Indoor HXs:	
	210 mm (length) × 190 mm	
Indoor HXs	(height) × 14 mm (width)	$\dot{Q}_{CO_2,air} = \sum_{j=1}^N (\eta_{fin} \alpha_{j,air,wall} A_j (T_{wall,j} - T_{air,j}) + \dot{m}_{cond,j} \cdot L_{vap})$
and Outdoor HX	230 mm (length) × 230 mm (height) × 14 mm (width)	
	Outdoor HX:	$= \sum_{j=1}^N \alpha_{j,CO_2,wall} A_j (T_{CO_2,j} - T_{wall,j})$
	660 mm (length) × 515 mm (height) × 16 mm (width)	
	Type: concentric tube	
	Length: 1600 mm	$\dot{Q}_{CO_2,CO_2} = \sum_{j=1}^N \alpha_{j,CO_2,CO_2} A_j (T_{CO_2,j,1} - T_{CO_2,j,2})$
IHX	Inside diameter: 16mm	$\alpha_{j,CO_2,CO_2} = \left( \frac{1}{\alpha_{CO_2,j,1}} + \frac{1}{\alpha_{CO_2,j,2}} \right)^{-1}$
	Outside diameter: 22mm	
	Type: Plate heat exchanger	$\dot{Q}_{CO_2,coolant} = \sum_{j=1}^N \alpha_{j,CO_2,coolant} A_j (T_{CO_2,j} - T_{coolant,j})$
Chiller	190 mm × 76 mm	$\alpha_{j,CO_2,coolant} = \left( \frac{1}{\alpha_{CO_2,j}} + \frac{1}{\alpha_{coolant,j}} \right)^{-1}$
	15 plates	

---

1

2 Where  $\dot{Q}_{CO_2,air}$  refers to the heat exchange rate between carbon dioxide and air, kW;  
3 N is the number of segments of heat exchanger; j is the index of each segment;  $\eta_{fin}$   
4 is the finned surface efficiency;  $\alpha_j$  is the heat transfer coefficient, kW/(m<sup>2</sup>·K);  $A_j$  is  
5 the surface areas, m<sup>2</sup>;  $L_{vap}$  is the latent vaporization heat of water, kW/kg;  $\dot{m}_{cond}$   
6 is the condensate mass flow rate, kg/s; The subscript "wall" designates the heat  
7 exchanger's tube wall;  $\dot{Q}_{CO_2,CO_2}$  refers to the heat exchange rate between two streams  
8 of CO<sub>2</sub> fluid (stream 1 and 2), kW;  $\dot{Q}_{CO_2,coolant}$  refers to the heat exchange rate  
9 between CO<sub>2</sub> and 50% aqueous solution of ethylene glycol, kW.

10 The heat transfer coefficient,  $\alpha_j$ , for CO<sub>2</sub> is determined using correlations from

1 various researchers: Dittus-Boelter's work is employed for both single-phase liquid and  
 2 single-phase vapor conditions [34]; Tang's correlations are applied for two-phase  
 3 condensation [35]; Gungor's findings serve for two-phase evaporation [36]; and Yoon's  
 4 research provides guidance for single-phase supercritical conditions [37]. For air,  $\alpha_j$   
 5 is evaluated using correlations presented by Chang and Wang [38], while the  $\alpha_j$  for  
 6 the coolant is calculated using the correlations presented by Dittus-Boelter [34].  
 7 Moreover, the pressure drop can be evaluated using the equations suggested by Cruz,  
 8 Coelho & Alves for Reynolds numbers below 2000 [39], and by Trinh for Reynolds  
 9 numbers exceeding 4000 [40]. In cases of transition regime, the friction factor  
 10 calculation employs linear interpolation between laminar and turbulent values  
 11 according to the given Reynolds number.

12

### 13 **2.2.2 Compressor model**

14 The compressor is a rolling rotor compressor with a capacity of 8.2cc. It is  
 15 modelled using the *CompPosDispRefrig* and *SpeedBoundaryRot* models.  
 16 *SpeedBoundaryRot* prescribes a constant or variable angular velocity on 1-D rotational  
 17 parts, it can be used to simulate a self-powered generic device. The  
 18 *CompPosDispRefrig* template represents a positive displacement, volumetric  
 19 efficiency based compressor. The outputs of this template are mass flow rate and  
 20 enthalpy change. The mass flow rate and power consumption are calculated as Eq. (1)  
 21 and Eq. (2) [41].

$$22 \quad \dot{m}_{CO_2} = V_d \cdot \dot{N}_{com} \cdot \rho_{suc} \cdot \eta_v(\varepsilon, \dot{N}_{com}, T_{suc}) \quad (1)$$

$$23 \quad \dot{W}_{com} = \dot{m}_{CO_2} \cdot \frac{h_{dis} - h_s}{\eta_{is}(\varepsilon, \dot{N}_{com}, T_{suc})} \cdot \frac{1}{\eta_e(\varepsilon)} \quad (2)$$

24 The data map for isentropic efficiency ( $\eta_{is}$ ), volumetric efficiency ( $\eta_v$ ) and motor  
 25 efficiency ( $\eta_e$ ) are derived from experimental data. These three parameters are jointly  
 26 determined by the compressor speed ( $\dot{N}_{com}$ ), pressure ratio ( $\varepsilon$ ) and compressor suction  
 27 temperature ( $T_{suc}$ ).  $V_d$  is the displacement of the compressor, m<sup>3</sup>;  $\rho_{suc}$  refers to the  
 28 suction density, kg/m<sup>3</sup>;  $h_s$  represents the enthalpy CO<sub>2</sub> at the suction state of the

1 compressor, kJ/kg.

2

### 3 **2.2.3 EEV model**

4 The throttle valves in this study used the *OrificeConn* model. This template  
5 models an orifice, defined by diameter or area and discharge coefficients, which  
6 calculates the mass flow rate between the adjacent flow volumes. The equation, as  
7 shown in Eq. (3), is solved to calculate the flow rate through the orifice [42-43].

$$8 \quad \dot{m}_{CO_2} = C_d \cdot A_{EEV} \cdot \sqrt{\frac{2\Delta P \cdot \rho_{EEV,in}}{k_{dp}}} \quad (3)$$

9 Where  $C_d$  is discharge coefficient, and  $A_{EEV}$  represents the circulation cross-  
10 sectional area of the EEV, m<sup>2</sup>;

11

### 12 **2.2.4 Other models**

13 The car cabin volume of 3.5 m<sup>3</sup> has been considered. The cabin's targeted  
14 temperature is 20 °C, and the model's specifications are mentioned in [12]. The  
15 accumulator with a capacity of 1.1 L is modeled by *AccumulatorRefrig*. The *Fan*  
16 module is used to simulate indoor/outdoor fans, and the efficiency information is taken  
17 from the map that the manufacturer supplies. *PID controllers* are also used to adjust  
18 the speed of the compressor and the indoor fan in addition to the areas of the two  
19 throttle valves.

20

## 21 **2.3 Verification of simulation models**

22 A test rig consistent with the model has been constructed, and a series of  
23 experiments are conducted to validate the accuracy of the model. The dimensions of  
24 all components are outlined in section 2.2. A photograph of the experimental setup is  
25 presented in Fig. 3. Additionally, all temperature, pressure, and flowrate sensors  
26 installed on the test rig are shown in Fig. 1. The details of the measurement equipment  
27 and associated errors are presented in Table 2. Notably, the experimental setup excludes  
28 the cabin and the PID controller used to regulate cabin temperature, instead opting to  
29 adjust the heat supply by directly varying the airflow.

1

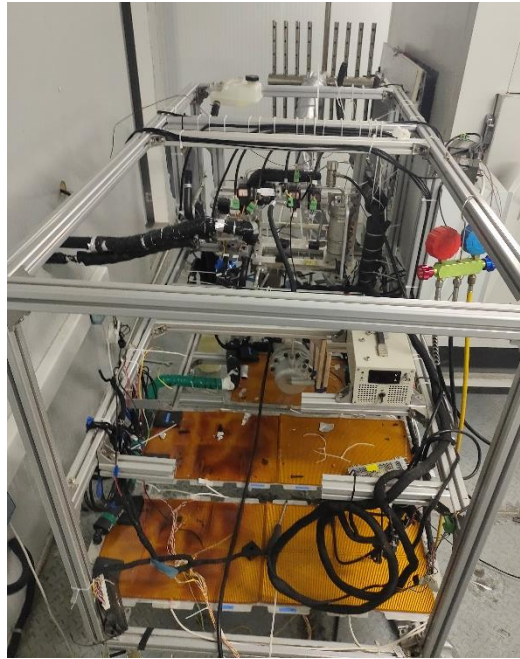


Fig.3. The photo of test rig.

2

3

4

5

6

Table 2

The parameters experimental measurement devices, and uncertainties.

Parameter	Component	Range and uncertainties
Air wet/dry bulb temperature	PT100 thermoelectrical resistance	-50~200 °C, $\pm (0.15 + 0.0002 \times \text{reading})$ °C
Coolant temperature	PT100 thermoelectrical resistance	-50~200 °C, $\pm (0.15 + 0.0002 \times \text{reading})$ °C
CO <sub>2</sub> fluid temperature	K-type thermocouple	-50~200 °C, $\pm 0.5$ °C
Pressure	MPM489 transmitter	0~20 MPa, 2.5 % of the range
Power	WT500	15~1000 V and 0.5~40 A, $\pm 0.1\%$ of reading + 0.1% of the range.
CO <sub>2</sub> Mass flow rate	Micro Motion Mass flowmeter	11500 kg·h <sup>-1</sup> , $\pm 1\%$
Coolant Mass flow rate	Turbine flowmeter	0.2~1.2m <sup>3</sup> /h, $\pm 0.5\%$

7

8

9

10

11

12

13

Two distinct chambers with differing enthalpy levels are employed for multiple steady-state experiments. Each enthalpy difference chamber possesses independent control over the immediate environment's temperature and humidity. Table 3 showcases the experimental test conditions.

Table 3

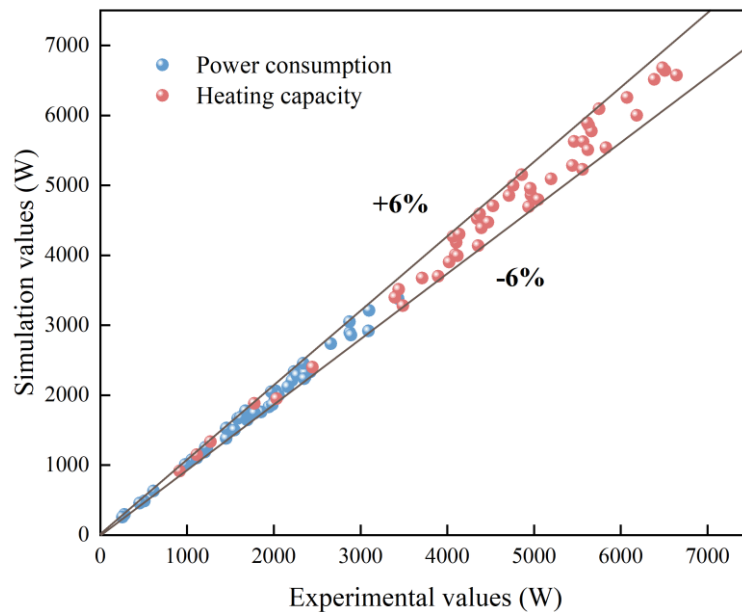
1 Detailed parameters of operation conditions.

Parameter	Values
Ambient temperature (°C)	-20, -10, 0, 7
Indoor HX inlet air temperature (°C)	-20, -10, 0, 20
Air flow rate (m <sup>3</sup> /h)	150,200,250,300
Coolant flow rate (L/min)	2,6,10

2

3 The error propagation for the cooling capacity was calculated using the Kline and  
4 McClintock [44] method. The largest uncertainty of the heating capacity was 3.83%.  
5 The simulation work was constructed to replicate the real-world conditions of the  
6 steady-state experiments. All the data's deviations for power consumption and heating  
7 capacity were within 6%, as displayed in Fig. 4, proving the validity of the simulation  
8 model.

9



10

11

Fig.4. The validity of the TMS simulation model.

12

## 13 2.4 Performance evaluation

14

15

The COP is the most crucial indicator for assessing the efficiency of heat pump systems [45]. COP for a heat pump used for cabin heating is

$$1 \quad COP_{cab} = \frac{\dot{Q}_{cab}}{\dot{W}_{com,cab}} = \frac{h_{dis} - h_{cab,out}}{h_{dis} - h_{suc}} \quad (4)$$

2 where  $\dot{Q}_{cab}$  and  $\dot{W}_{com,cab}$  are the cabin heating rate and compressor power  
3 consumption to heat the cabin, kW;  $h_{dis}$ ,  $h_{suc}$  and  $h_{c,out}$  are the enthalpy at the  
4 compressor discharge point, the enthalpy at the compress  
5 or suction point and the enthalpy of the CO<sub>2</sub> fluid after heating the cabin, respectively.

6 COP for a heat pump used to battery heating is

$$7 \quad COP_{bat} = \frac{\dot{Q}_{bat}}{\dot{W}_{com,bat}} = \frac{h_{dis} - h_{bat,out}}{h_{dis} - h_{suc}} \quad (5)$$

8 where  $\dot{Q}_{bat}$  and  $\dot{W}_{com,bat}$  are the battery heating rate and compressor power  
9 consumption to heat the battery, kW;  $h_{dis}$ ,  $h_{suc}$  and  $h_{bat,out}$  are the enthalpy at the  
10 compressor discharge point, the enthalpy at the compressor suction point and the  
11 enthalpy of the CO<sub>2</sub> fluid after heating the battery, respectively.

12 The percentage of CO<sub>2</sub> flow rate used to heat the battery is defined as,

$$13 \quad k = \frac{\dot{m}_{bat}}{\dot{m}_{cab} + \dot{m}_{bat}} \quad (6)$$

14 The performance factor of a thermal management system is defined as,

$$15 \quad COP_{TMS} = \frac{\dot{Q}_{cab} + \dot{Q}_{bat}}{\dot{W}_{com}} = \frac{\dot{m}_{cab} \cdot (h_{dis} - h_{cab,out}) + \dot{m}_{bat} \cdot (h_{dis} - h_{bat,out})}{(\dot{m}_{cab} + \dot{m}_{bat}) \cdot (h_{dis} - h_{suc})}$$

$$16 \quad = (1 - k) \cdot COP_{cab} + k \cdot COP_{bat} \quad (7)$$

17 The COP<sub>TMS</sub> is dependent on the COP<sub>cab</sub> and COP<sub>bat</sub> as well as the mass flow rate  
18 of the two sub-circulations, as can be seen from Eq. (7).

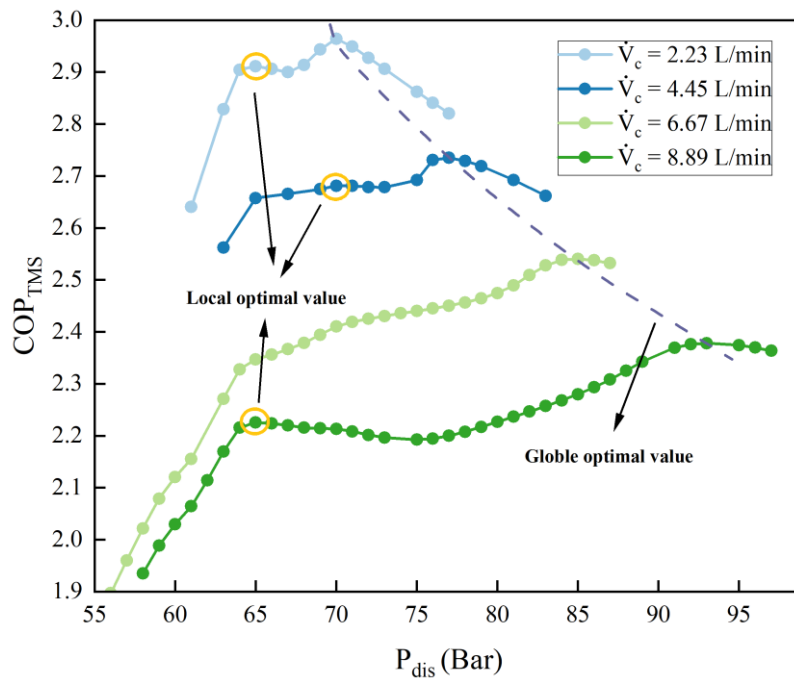
19

## 20 **3 Results and discussions**

### 21 **3.1 Influence of coolant flow rate**

22 Fig. 5 shows the variation of COP<sub>TMS</sub> with discharge pressure for coolant flow  
23 rates ( $\dot{V}_c$ ) from 2.23 to 8.89 L/min (Ambient temperature T<sub>a</sub>=-20 °C, HVAC inlet air  
24 temperature T<sub>air,in</sub>=-10 °C, chiller coolant inlet temperature T<sub>c,in</sub>=25 °C). As can be seen,  
25 as  $\dot{V}_c$  increases, the optimal COP<sub>TMS</sub> decays by 19.8%, going from 2.964 to 2.378.  
26 Moreover, as  $\dot{V}_c$  rises, there is a corresponding rise in the optimal P<sub>dis</sub>. These

1 phenomena find their roots in the heightened heating load placed on the battery, leading  
 2 to elevated CO<sub>2</sub> fluid temperatures at the chiller outlet and an elevation in compressor  
 3 speed. The CO<sub>2</sub> TMS nevertheless promises a competitive energy efficiency in spite of  
 4 the challenging working circumstances at -20 °C. This is noteworthy considering the  
 5 efficiency of the most used Positive Temperature Coefficient (PTC) heaters is only 0.9  
 6 [46]. Although it can be determined that the TMS has an overall optimal discharge  
 7 pressure, the COP does not always increase and subsequently decrease with P<sub>dis</sub> as in  
 8 conventional systems (just one maximum point) [27]. To describe these causes, the  
 9 optimal discharge pressures for the battery heating cycle and the cabin air heating cycle  
 10 are used as benchmarks to divide the variation of COP<sub>TMS</sub> with P<sub>dis</sub> into three stages  
 11 (as shown in Fig. 6): the first stage is before the peak COP<sub>cab</sub> is reached; the second  
 12 stage is after the peak COP<sub>cab</sub> is reached but before the peak COP<sub>bat</sub> is reached; and the  
 13 third stage is after the peak COP<sub>bat</sub> is reached. In addition, we define the discharge  
 14 pressure that maximizes COP<sub>TMS</sub> as the "global optimal discharge pressure." On the  
 15 other hand, when the system does not reach its maximum COP<sub>TMS</sub> at a particular  
 16 discharge pressure but exhibits a trend of COP<sub>TMS</sub> initially increasing and then  
 17 decreasing with changes in discharge pressure around this value, we define that  
 18 discharge pressure as a "local optimal discharge pressure."





1 Fig.5. Variation of COP<sub>TMS</sub> with P<sub>dis</sub> at different  $\dot{V}_c$ .

2  
3 Due to the limited enthalpy difference between the CO<sub>2</sub> chiller's outlet and inlet,  
4 the k-value in stage I is at a high level as shown in Fig.6. According to the lgP-h  
5 diagrams, the system is in a subcritical cycle during stage I, where the CO<sub>2</sub> condensing  
6 temperature is lower than the coolant temperature. There is a gradual increase in  
7 enthalpy difference as the P<sub>dis</sub> rises because the CO<sub>2</sub> at the chiller outlet is superheated  
8 vapor. In addition, the rising COP<sub>cab</sub> /COP<sub>bat</sub> values and the relatively stable k values  
9 lead to a continuous increase in COP<sub>TMS</sub>.

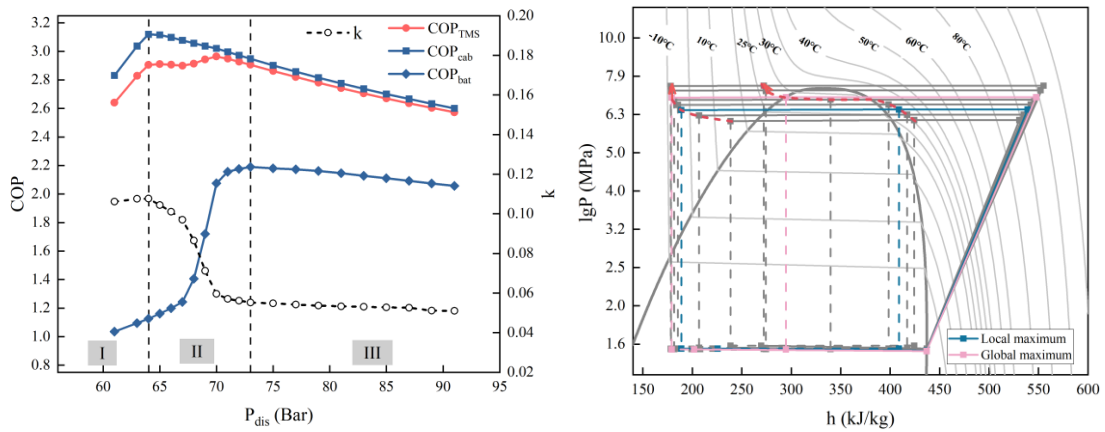
10 At stage II, the k value decreased rapidly and the decreasing trend tends to level  
11 off gradually. This is due to the rapid increase in the enthalpy difference between the  
12 chiller. The increase enthalpy difference is caused by the enhanced heat transfer  
13 coefficient in the chiller as well as the increase in the slope of the CO<sub>2</sub> isotherm. In  
14 addition, COP<sub>bat</sub> increases with the increase of P<sub>dis</sub>, and its growth rate decreases with  
15 the increase of the  $\dot{V}_c$ . The explanation is as follows: when  $\dot{V}_c=2.23$  L/min, the chiller  
16 can ensure good heat transfer capacity in the subcritical zone, and under the near  
17 isothermal condition, the enthalpy difference rises dramatically with an increase in P<sub>dis</sub>.  
18 The chiller outlet temperature rises above the CO<sub>2</sub> critical temperature as  $\dot{V}_c$  increases.  
19 With rising temperatures, the isotherm's slope declines, which causes COP<sub>bat</sub> to develop  
20 more slowly. This is clearly illustrated in the four lgP-h plots depicted in Fig. 6.

21 The k value is kept at a low level and tends to slowly decline in stage III. This is  
22 brought on by the gradually rising enthalpy difference in indoor HXs and chiller.  
23 Moreover, COP<sub>TMS</sub> decreases when P<sub>dis</sub> increases since COP<sub>bat</sub> and COP<sub>cab</sub> decline. In  
24 conclusion, it is evident that for COP<sub>TMS</sub> to be maximized in stage II, there is at least  
25 one optimal discharge pressure value that leads to the maximum COP<sub>TMS</sub>.

26 When  $\dot{V}_c=2.23$  L/min and  $\dot{V}_c=4.45$  L/min, the COP<sub>TMS</sub> rises to the local  
27 maximum point and subsequently to the global maximum point in stage II. This can be  
28 explained by the fact that the initial value of k is at a high level, thus the rise of COP<sub>bat</sub>  
29 plays a dominant role. The value of k then falls as P<sub>dis</sub> rises, which causes a decline in

1 COP<sub>cab</sub> as the main factor affecting the COP<sub>TMS</sub>. Until COP<sub>bat</sub> rises significantly, the  
 2 COP<sub>TMS</sub> global optimum is apparent. At  $\dot{V}_c = 6.67$  L/min, COP<sub>TMS</sub> increases and then  
 3 decreases with the rise of P<sub>dis</sub> in stage II, thus there exists only one optimal value. This  
 4 is brought on by both the growing COP<sub>bat</sub> and the overall greater k value. The local  
 5 optimum P<sub>dis</sub> occurs at the optimal value of COP<sub>cab</sub> at  $\dot{V}_c = 8.89$  L/min. Even if k has a  
 6 large value, the COP<sub>bat</sub> develops very slowly, creating a local optimum point.

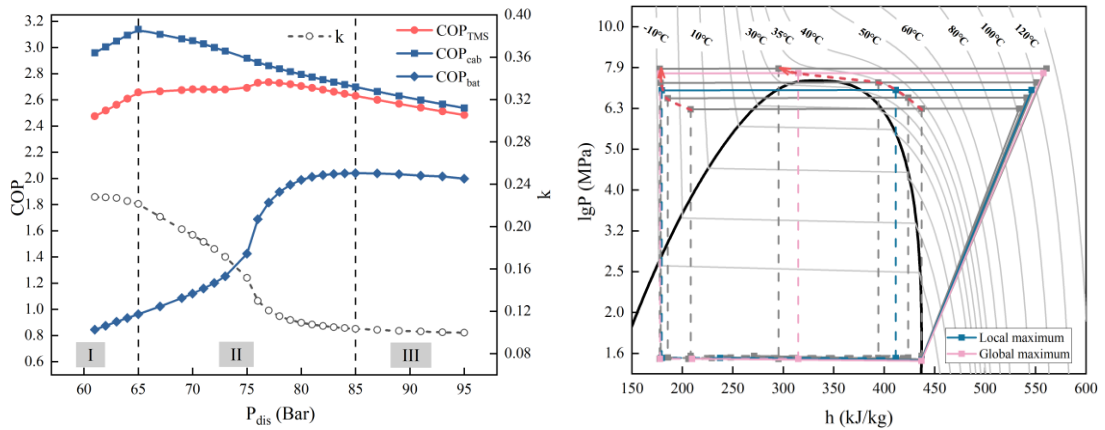
7 In general, in addition to the global optimal point, other local maximum points  
 8 may still exist within stage II. The existence of a local maximum point is determined  
 9 by the combination of the k value and the rising rate of COP<sub>bat</sub>.



10

11

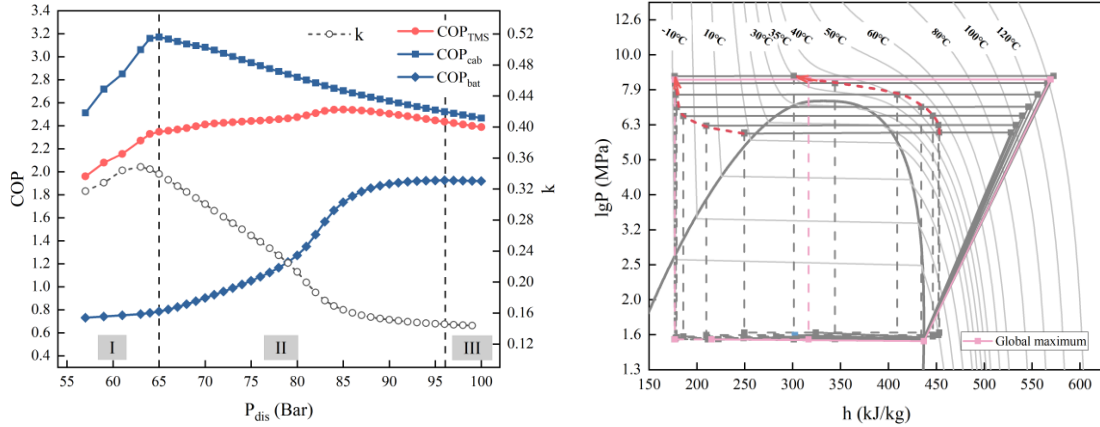
(a)  $\dot{V}_c = 2.23$  L/min



12

13

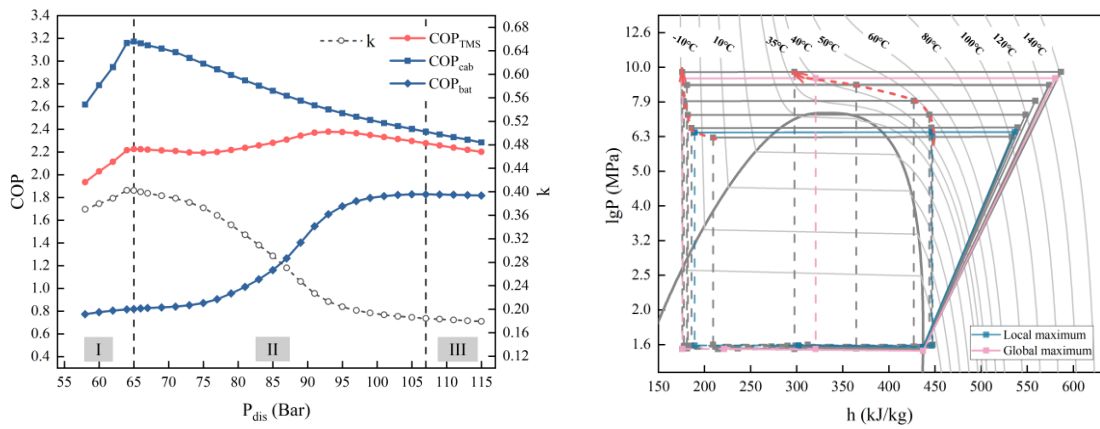
(b)  $\dot{V}_c = 4.45$  L/min



1

2

(c)  $\dot{V}_c = 6.67$  L/min



3

4

(d)  $\dot{V}_c = 8.89$  L/min

5

Fig.6. Trends of  $COP_{TMS}$ ,  $COP_{cab}$ ,  $COP_{bat}$  and  $k$  at different stages as well as  $lgP$ - $h$  diagrams.

6

7

8

### 3.2 Influence of chiller inlet coolant temperature

9

Fig. 7 shows the variation of the  $COP_{TMS}$  with  $P_{dis}$  for  $T_a = -20$  °C and  $T_{air,in} = -10$  °C.

10

It can be seen the optimal  $P_{dis}$  increases from 87 to 97 Bar as chiller inlet coolant

11

temperature ( $T_{c,in}$ ) increases from 20 °C to 30 °C at  $\dot{V}_c = 8.89$  L/min, but the  $COP_{TMS,opt}$

12

decreases from 2.500 to 2.277, a 8.9% reduction. This is due to the increase in the

13

chiller outlet  $CO_2$  temperature and the high  $k$  value. At  $\dot{V}_c = 8.89$  L/min, the local

14

optimum  $P_{dis}$  exists at the optimal value of 65 Bar as  $T_{c,in}$  increases from 20 °C to 30 °C,

15

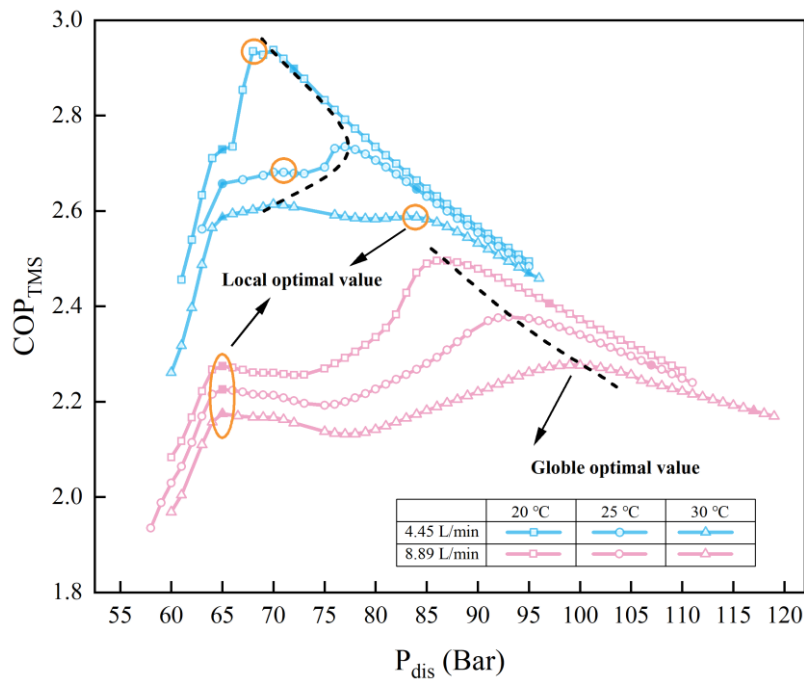
which is also the optimal value of  $COP_{cab}$ . However, At  $\dot{V}_c = 4.45$  L/min, the optimal

16

$P_{dis}$  increases and then decreases with the increase of  $T_{c,in}$ . This is due to a slower

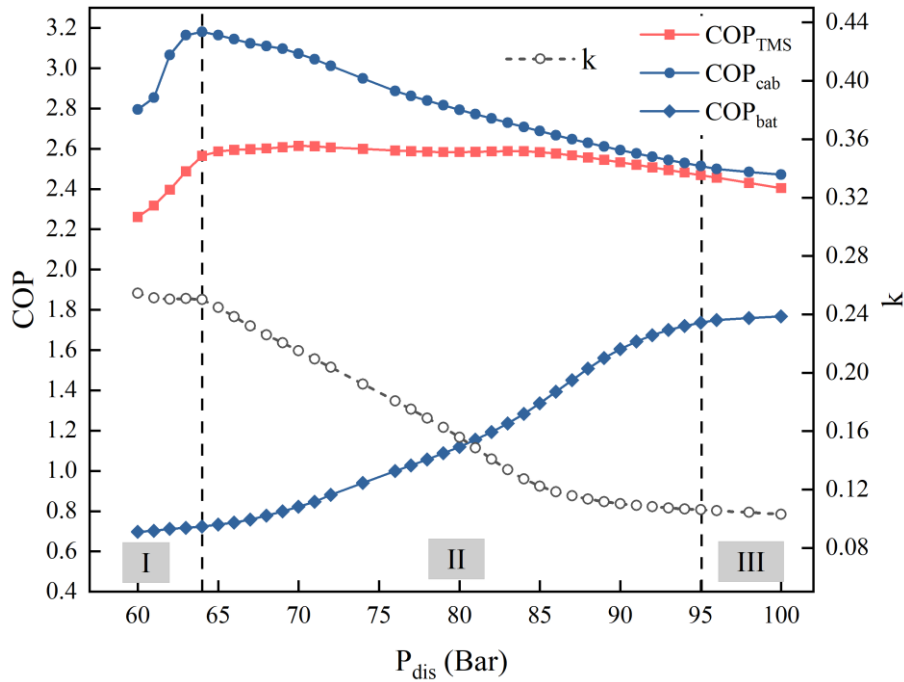
1 COP<sub>bat</sub> increase in the stage II caused by the high CO<sub>2</sub> temperature at the chiller outlet  
 2 (as shown in Fig. 8). At T<sub>c,in</sub>=30 °C, the P<sub>pse-opt</sub> value is 71 Bar and the maximum  
 3 COP<sub>TMS</sub> is 2.614, while the local optimal discharge pressure value is 83 Bar and the  
 4 local maximum COP<sub>TMS</sub> is 2.589. The global optimum COP<sub>TMS</sub> is only 0.97% higher  
 5 than the local optimum value.

6  
7



8  
9  
10

Fig.7. Variation of COP<sub>TMS</sub> with P<sub>dis</sub> at different T<sub>c,in</sub>.



1

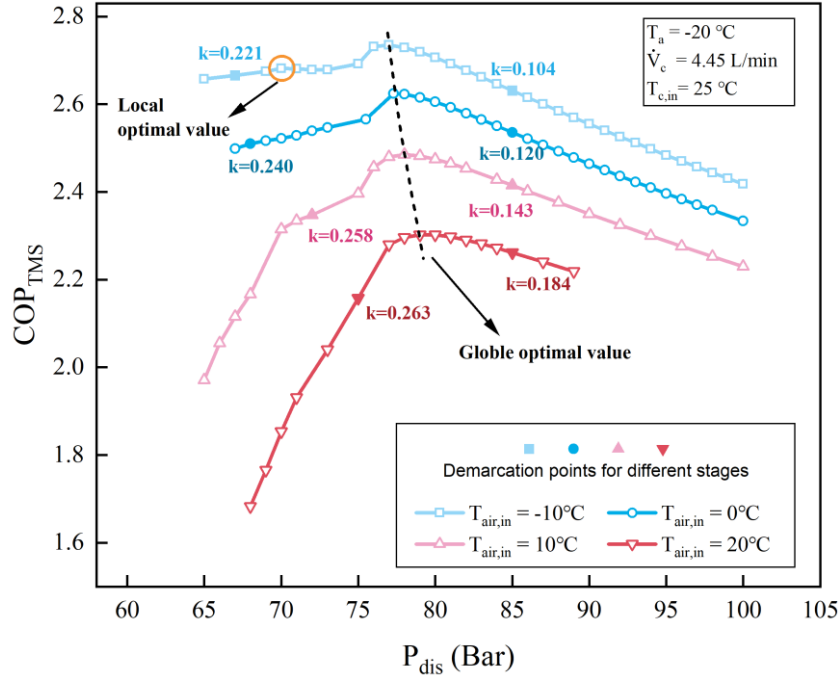
2 Fig.8. Trends of  $COP_{TMS}$ ,  $COP_{cab}$ ,  $COP_{bat}$  and  $k$  at different stages ( $\dot{V}_c=4.45$  L/min,  
3  $T_{c,in}=30$  °C)

4

### 5 3.3 Influence of HVAC inlet air temperature

6 Fig. 9 depicts the variation of  $COP_{TMS}$  concerning  $P_{dis}$  for HVAC inlet air  
7 temperatures ( $T_{air,in}$ ) ranging from  $-10^\circ\text{C}$  to  $20^\circ\text{C}$ . It is evident that the parameter  $k$   
8 increases proportionally with the elevation of  $T_{air,in}$ . This phenomenon can be attributed  
9 to the reduction in heating demands within the cabin. Furthermore, there is a  
10 noteworthy decrease in the maximum  $COP_{TMS}$  value, dropping from 2.735 to 2.302,  
11 representing a substantial 15.8% reduction as  $T_{air,in}$  increases from  $-10^\circ\text{C}$  to  $20^\circ\text{C}$ . This  
12 reduction can be attributed to the fact that, despite the increased heating load required  
13 when  $T_{air,in}$  is  $-10^\circ\text{C}$ , the system experiences enhanced efficiency due to the lower  $CO_2$   
14 outlet temperature from the indoor HXs. Besides, a local optimum  $P_{dis}$  exists only at  
15 inlet air temperature of  $-10$  °C, which is due to the small  $k$  values.

16



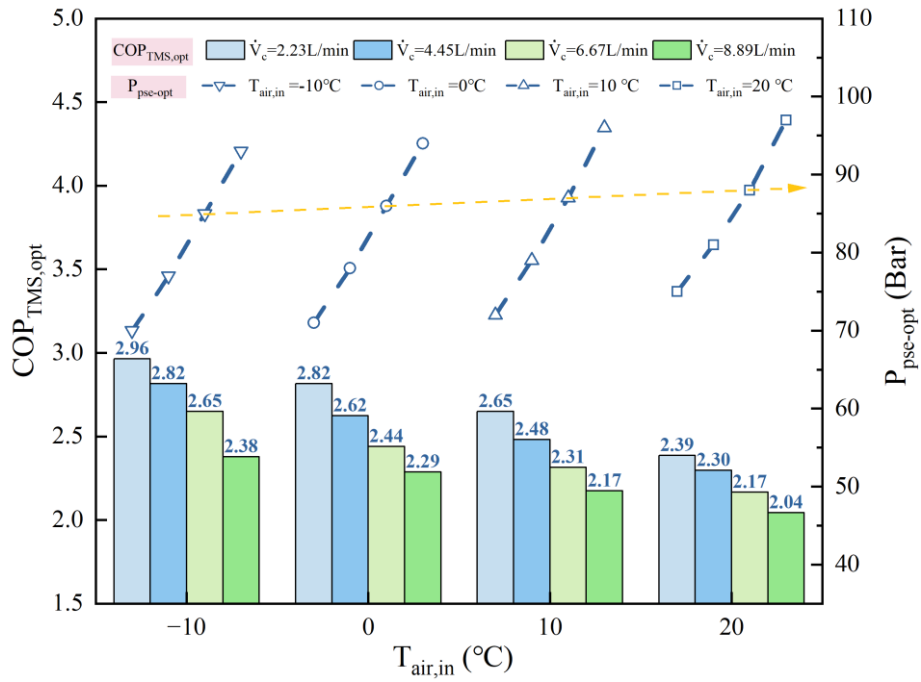
1  
2

Fig.9. Variation of  $COP_{TMS}$  at different  $T_{air,in}$ .

3

4 Fig.10. shows the values of  $COP_{TMS,opt}$  and  $P_{dis,opt}$  for  $T_{air,in}$  increases from  $-10\text{ }^{\circ}\text{C}$   
5 to  $20\text{ }^{\circ}\text{C}$  ( $T_a=-20\text{ }^{\circ}\text{C}$ ,  $T_{c,in}=25\text{ }^{\circ}\text{C}$ ,  $\dot{V}_c=2.23\text{ L/min}\sim 8.89\text{ L/min}$ ). Contrary to the typical  
6 heat pump system for cabin heating, there have little effect of  $T_{air,in}$  on the optimal  
7 discharge pressure, with a 3~5 bar change from  $-10\text{ }^{\circ}\text{C}$  to  $20\text{ }^{\circ}\text{C}$ . However, as  $\dot{V}_c$   
8 increases from  $2.23\text{ L/min}$  to  $8.89\text{ L/min}$ , there is a corresponding increase in  $P_{dis,opt}$  by  
9 approximately 22 to 24 bar. Therefore, it becomes evident that  $\dot{V}_c$  exerts a more  
10 pronounced influence on the global optimal discharge pressure than  $T_{air,in}$ . This  
11 phenomenon arises due to the fact that the  $CO_2$  fluid temperature at the chiller outlet is  
12 higher than that at the indoor heat exchanger outlet. This results in a steeper slope of  
13 the isotherms on one hand and, on the other hand, when  $COP_{TMS}$  reaches its optimum  
14 value, the indoor HXs' heat transfer capacity is already approaching its optimal state,  
15 while the chiller's heat transfer capacity increases rapidly with an increase in discharge  
16 pressure. Conversely,  $T_{air,in}$  exhibits a more significant effect on  $COP_{TMS}$ , especially in  
17 scenarios where  $\dot{V}_c=2.23\text{ L/min}$ . This is primarily attributed to the fact that the heating  
18 load predominantly originates from the cabin. When  $T_{air,in}$  is  $-10\text{ }^{\circ}\text{C}$ ,  $COP_{TMS}$   
19 experiences an increase of 16.29% to 24.21% compared to the case where  $T_{air,in}$  is  $20\text{ }^{\circ}\text{C}$ .

1  
2



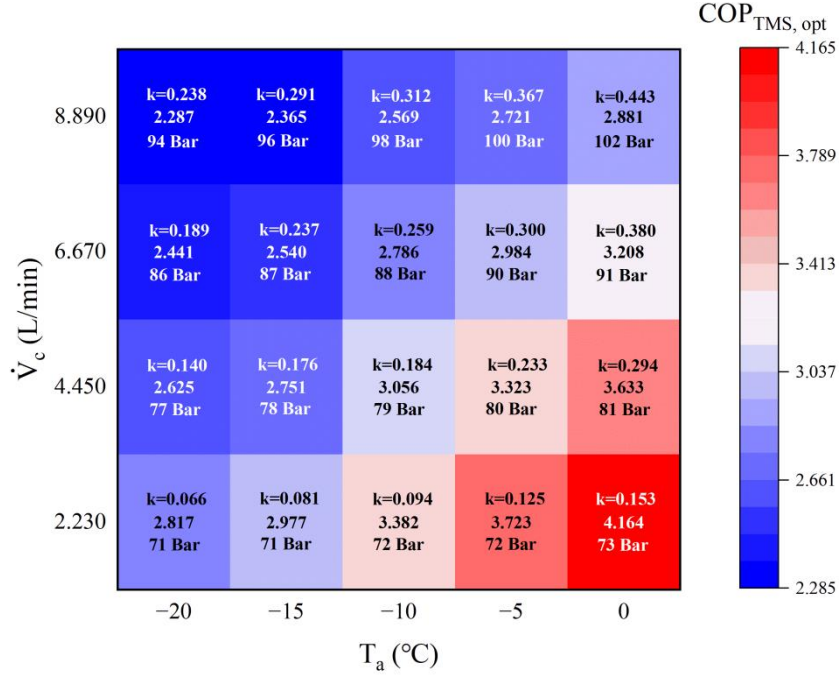
3  
4  
5

Fig.10.  $COP_{TMS,opt}$  and  $P_{dis,opt}$  values in different  $T_{air,in}$ .

### 6 3.4 Influence of ambient temperature

7 According to Fig. 11, when the ambient temperature rose from -20 °C to 0 °C, the  
 8 global optimal discharge pressure only increased by 2~8 Bar at constant  $\dot{V}_c$  ( $T_{air,in}=0$  °C,  
 9  $T_{c,in}=25$  °C). In contrast,  $\dot{V}_c$  increases from 2.23 L/min to 8.89 L/min, the global  
 10 optimal discharge pressure increases by 23~29 Bar at the same  $T_a$ . Thus  $\dot{V}_c$  has a  
 11 greater effect on the optimal  $P_{dis}$  compared to the ambient temperature. However, the  
 12 ambient temperature has a significant effect on the  $COP_{TMS,opt}$  values. In addition, the  
 13 optimal  $k$  value increases with the increase of  $T_a$ , which is caused by the decrease of  
 14 cabin heating load.

15



1

2

Fig.11.  $COP_{TMS, opt}$  and  $P_{dis, opt}$  values in different  $T_a$ .

3

4

In summary, there must be an optimal exhaust pressure for the cabin-and-battery mixed heating mode to maximize the  $COP_{TMS}$ , which is determined by both the heat transfer capacity limit and the isotherm slope, regardless of the system state of subcritical or transcritical cycles. Therefore, the discharge pressure that maximizes the  $COP_{TMS}$  can be referred to as the pseudo-optimal discharge pressure ( $P_{pse-opt}$ ). In an EV with a cabin volume of  $3.5 \text{ m}^3$ , coolant flow rate  $\dot{V}_c$ , chiller inlet coolant temperature  $T_{c,in}$ , HVAC inlet air temperature  $T_{air,in}$  and ambient temperature  $T_a$  are all factors that affect the  $P_{pse-opt}$ . Among them,  $\dot{V}_c$  and  $T_{c,in}$  are more important influencing factors. In this study, a predictive equation (Eq. (8)) for  $P_{pse-opt}$  was obtained using Response Surface Analysis [47]. As can be seen from Fig. 12, the prediction deviation is within 5%.

15

$$P_{pse-opt} = T_a(-0.0234T_a + 0.0545T_{c,in} - 1.6643) + 1.9356T_{c,in} + 3.7113\dot{V}_c$$

16

$$+T_{air,in}(-0.0402T_{c,in} - 0.0288\dot{V}_c + 1.3986) + 14.5906 \quad (8)$$



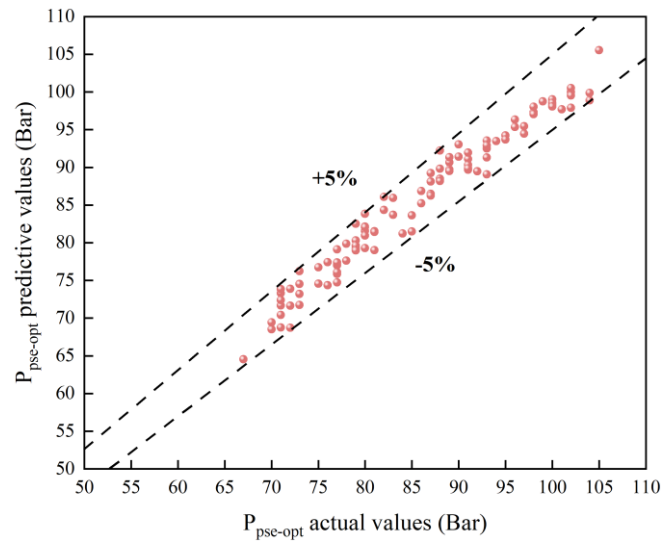


Fig.12. Comparison of actual values and calculated values.

#### Conclusion

This paper investigates the system characteristics of the CO<sub>2</sub> thermal management system in cabin-and-battery mixed heating mode in winter. We built a liquid-cooled CO<sub>2</sub> TMS test rig and corresponding simulation model. Additionally, numerous PI controllers and a cabin thermal model were combined to fully analyze the winter performance of the CO<sub>2</sub> liquid-cooled TMS. The main conclusions are as follows:

- (1) The optimal discharge pressures for the battery heating cycle and the cabin air heating cycle are used as benchmarks to divide the variation of COP<sub>TMS</sub> with P<sub>dis</sub> into three stages. There is a pseudo-optimal discharge pressure to maximize the COP<sub>TMS</sub> in stage II regardless of the system state of subcritical or transcritical cycles.
- (2) In addition to the P<sub>pse-opt</sub>, other local maximum points may still exist within stage II. The existence of a local maximum point is determined by the combination of the k value and the rising rate of COP<sub>bat</sub>.
- (3) When T<sub>a</sub>=-20 °C, T<sub>c,in</sub>=30 °C,  $\dot{V}_c=8.89$  L/min and T<sub>air,in</sub>=-10 °C, the COP<sub>TMS,opt</sub> is 2.277, which significantly outperforms the conventional PTC heaters with an efficiency as low as 0.9. This comparison solidifies the proof that the CO<sub>2</sub> TMS demonstrates a competitive energy efficiency despite the demanding operational

1 conditions.

2 (4) The  $P_{pse-opt}$  increases with the increase of  $T_{air,in}$ ,  $T_a$  and  $\dot{V}_C$ . However, the variation  
3 pattern of  $P_{pse-opt}$  with  $T_{c,in}$  varies under different battery heating loads. A  $P_{pse-opt}$   
4 prediction equation is proposed for maximizing the performance of CO<sub>2</sub> thermal  
5 management system in cabin-and-battery mixed heating mode for winter. It  
6 presents a solution for the optimal control of the CO<sub>2</sub> thermal management system.

7

## 8 **Acknowledgments**

9 The corresponding author is grateful to the Foundation for Innovative Research  
10 Groups of the National Natural Science Foundation of China (No.51721004), the  
11 National Natural Science Foundations of China (No.52006161) and China Scholarship  
12 Council (No. 202206280214).

13

## 14 **References**

- 15 [1] G. Xia, L. Cao, G. Bi, A review on battery thermal management in electric vehicle  
16 application, *Journal of Power Sources*, 2017, 367, 90-105.
- 17 [2] P. V. Chombo, Y. Laonual, A review of safety strategies of a Li-ion battery, *Journal*  
18 *of Power Sources*, 2020, 478, 228649.
- 19 [3] Y. Wang, J. Wu, Thermal performance predictions for an HFE-7000 direct flow  
20 boiling cooled battery thermal management system for electric vehicles, *Energy*  
21 *Conversion and Management*, 2020, 207, 112569.
- 22 [4] Q. Wang, B. Jiang, B. Li, Y. Yan, A critical review of thermal management models  
23 and solutions of lithium-ion batteries for the development of pure electric vehicles,  
24 *Renewable and Sustainable Energy Reviews*, 2016, 64, 106-128.
- 25 [5] W. Ca, C. Zhao, Y. Wang, T. Dong, F. Jiang, Thermal modeling of full-size-scale  
26 cylindrical battery pack cooled by channeled liquid flow, *International Journal of Heat*  
27 *and Mass Transfer*, 2019, 138, 1178-1187.
- 28 [6] Y. Fan, Z. Wang, T. Fu, H. Wu, Numerical investigation on lithium-ion battery  
29 thermal management utilizing a novel tree-like channel liquid cooling plate exchanger,

- 1 International Journal of Heat and Mass Transfer, 2022, 183, Part B, 122143.
- 2 [7] Z. An, C. Zhang, Y. Luo, J. Zhang, Cooling and preheating behavior of compact  
3 power Lithium-ion battery thermal management system, Applied Thermal Engineering,  
4 2023, 226, 120238.
- 5 [8] A. Alahmer, A. Mayyas, A. A. Mayyas, M.A. Omar b, D. Shan, Vehicular thermal  
6 comfort models; a comprehensive review, Applied Thermal Engineering, 2011, 31(6–  
7 7), 995-1002.
- 8 [9] J. H. Ahn, J. S. Lee, C. Baek, Y. Kim, Performance improvement of a  
9 dehumidifying heat pump using an additional waste heat source in electric vehicles  
10 with low occupancy, Energy, 2016, 115(15) ,67-75.
- 11 [10] M. H. Park, S. C. Kim, Heating Performance Characteristics of High-Voltage PTC  
12 Heater for an Electric Vehicle, Energies, 2017, 10(10), 1494.
- 13 [11] S. H. Hong, D. S. Jang, S. Yun, Jae H. Baek, Y. Kim, Performance improvement  
14 of heat pumps using novel microchannel heat exchangers with plain-louver fins during  
15 periodic frosting and defrosting cycles in electric vehicles, Energy Conversion and  
16 Management, 2020, 223, 113306.
- 17 [12] H. Wang, F. Cao, F. Jia, Y. Song, X. Yin, Potential assessment of transcritical CO<sub>2</sub>  
18 secondary loop heat pump for electric vehicles, Applied Thermal Engineering, 2023,  
19 224, 119921.
- 20 [13] M. Hosoz, M. Direk, Performance evaluation of an integrated automotive air  
21 conditioning and heat pump system, Energy Conversion and Management, 2006, 47  
22 (5), 545-559.
- 23 [14] K. Zhang, M. Li, C. Yang, Z. Shao, L. Wang, Exergy Analysis of Electric Vehicle  
24 Heat Pump Air Conditioning System with Battery Thermal Management System,  
25 Journal of Thermal Science, 2020, 29, 408–422.
- 26 [15] J. Cen, Z. Li, F. Jiang, Experimental investigation on using the electric vehicle air  
27 conditioning system for lithium-ion battery thermal management, Energy for  
28 Sustainable Development, 2018, 45, 88-95.
- 29 [16] S. Park, D.S. Jang, D.C. Lee, S. H. Hong, Y. Kim, Simulation on cooling

- 1 performance characteristics of a refrigerant-cooled active thermal management system  
2 for lithium-ion batteries, *International Journal of Heat and Mass Transfer*, 2019, 135,  
3 131-141.
- 4 [17] J. Cen, F. Jiang, Li-ion power battery temperature control by a battery thermal  
5 management and vehicle cabin air conditioning integrated system, *Energy for*  
6 *Sustainable Development*, 2020, 57, 141-148.
- 7 [18] X. Tang, Q. Guo, M. Li, C. Wei, Z. Pan, Y. Wang, Performance analysis on liquid-  
8 cooled battery thermal management for electric vehicles based on machine learning,  
9 *Journal of Power Sources*, 2021, 494, 229727.
- 10 [19] M. Shen, Q. Gao. System simulation on refrigerant-based battery thermal  
11 management technology for electric vehicles, *Energy Conversion and Management*,  
12 2020, 203, 112176.
- 13 [20] Z. Tian, W. Gan a, X. Zhang, B. Gu, L. Yang, Investigation on an integrated  
14 thermal management system with battery cooling and motor waste heat recovery for  
15 electric vehicle, *Applied Thermal Engineering*, 2018, 136, 16-27.
- 16 [21] J. Guo, F. Jiang, A novel electric vehicle thermal management system based on  
17 cooling and heating of batteries by refrigerant, *Energy Conversion and Management*,  
18 2021, 237, 114145.
- 19 [22] UNIDO. The Montreal protocol evolves to fight climate change, 2016.
- 20 [23] H. Wang, Y. Song, Y. Qiao, S. Li, F. Cao, Rational assessment and selection of air  
21 source heat pump system operating with CO<sub>2</sub> and R407C for electric bus, *Renewable*  
22 *Energy*, 2022, 182, 86-101.
- 23 [24] J. Dong, Y. Wang, S. Jia, X. Zhang, L. Huang, Experimental study of R744 heat  
24 pump system for electric vehicle application, *Applied Thermal Engineering*, 2021, 183,  
25 116191.
- 26 [25] D. Wang, B. Yu, W. Li, J. Shi, J. Chen, Heating performance evaluation of a CO<sub>2</sub>  
27 heat pump system for an electrical vehicle at cold ambient temperatures, *Applied*  
28 *Thermal Engineering*, 2018, 142, 656-664.
- 29 [26] S.M. Liao, T.S. Zhao, A. Jakobsen, A correlation of optimal heat rejection

1 pressures in transcritical carbon dioxide cycles, *Applied Thermal Engineering*, 2000,  
2 20(9), 831-841.

3 [27] A. Wang, F. Cao, X. Yin, F. Jia, J. Fang, X. Wang, Pseudo-optimal discharge  
4 pressure analysis of transcritical CO<sub>2</sub> electric vehicle heat pumps due to temperature  
5 glide, *Applied Thermal Engineering*, 2022, 215, 118856.

6 [28] X. Yin, J. Fang, A. Wang, Y. Song, F. Cao, X. Wang, A novel CO<sub>2</sub> thermal  
7 management system with battery two-phase (evaporative) cooling for electric vehicles,  
8 *Results in Engineering*, Volume 16, December 2022, 100735.

9 [29] A. Wang, X. Yin, Z. Xin, F. Cao, Z. Wu, B. Sundén, D. Xiao, Performance  
10 optimization of electric vehicle battery thermal management based on the transcritical  
11 CO<sub>2</sub> system, *Energy*, Volume 266, 1 March 2023, 126455

12 [30] H. Wang, W. Wang, Y. Song, X. Yang, P. Valdiserri, E. Rossi di Schio, G. Yu, F.  
13 Cao, Data-driven model predictive control of transcritical CO<sub>2</sub> systems for cabin  
14 thermal management in cooling mode, *Applied Thermal Engineering*, 2023, 235, 25  
15 121337.

16 [31] X. Li, H. Tian, G. Shu, M. Zhao, C. N. Markides, C. Hu, a Potential of carbon  
17 dioxide transcritical power cycle waste-heat recovery systems for heavy-duty truck  
18 engines, *Applied Energy*, 2019, 250, 15,1581-1599.

19 [32] R. Zhao, H. Zhang, S. Song, F. Yang, X. Hou, Y. Yang, Global optimization of the  
20 diesel engine–organic Rankine cycle (ORC) combined system based on particle swarm  
21 optimizer (PSO), *Energy Conversion and Management*, 2018, 174 (15), 248-259.

22 [33] M. N. Nabi, B. Ray, F. Rashid, W. A. Hussam, S.M. M, Parametric analysis and  
23 prediction of energy consumption of electric vehicles using machine learning, *Journal*  
24 *of Energy Storage*, 2023, 72, Part B, 20, 108226.

25 [34] F. W. Dittus, L. M. K. Boelter, Heat transfer in automobile radiators of the tubular  
26 type, *University of California Publications of Engineering*, 1930, 2, 443-61.

27 [35] L. Tang, M. M. Ohadi, A.T. Johnson, Flow Condensation in Smooth and Micro-  
28 fin Tubes with HCFC-22, HFC-134a and HFC-410A Refrigerants. *Journal of Enhanced*  
29 *Heat Transfer*, 2000, 7, 289-326.

- 1 [36] K. E. Gungor, R. H. S. Winterton, Simplified general correlation for saturated flow  
2 boiling and comparisons of correlations with data, *Chemical engineering research &*  
3 *design*, 1987, 65(2), 148-156.
- 4 [37] S. H. Yoon, J. H. Kim, Y. W. Hwang, M. S. Kim, K. Min, Y. Kim, Heat transfer  
5 and pressure drop characteristics during the in-tube cooling process of carbon dioxide  
6 in the supercritical region, *International Journal of Refrigeration*, 2003, 26, 857–864.
- 7 [38] Y. J. Chang, C. C. Wang, A generalized heat transfer correlation for louver fin  
8 geometry, *Heat Mass Transfer*, 1997, 40, 533-544.
- 9 [39] D. A. Cruz, P. M. Coelho, M. A. Alves, A simplified method for calculating heat  
10 transfer coefficients and friction factors in laminar pipe flow of non-newtonian fluids,  
11 *Journal of Heat Transfer*, 2012, 134.
- 12 [40] K. T. Trinh, The wall shear rate in non-Newtonian turbulent pipe flow, *Physics*,  
13 2010.
- 14 [41] B.D. Rasmussen, A. Jakobsen, Review of Compressor Models and Performance  
15 Characterizing Variables, in: *International Compressor Engineering Conference*, 2000,  
16 paper 1429.
- 17 [42] B. Munson, D. Young, *Fundamentals of Fluid Mechanics*, 4th Edition, John Wiley  
18 and Sons, Inc., New York, 2002.
- 19 [43] S. Sisavath, X. Jing, C. C. Pain, R. W. Zimmerman, Creeping Flow Through an  
20 Axisymmetric Sudden Contraction or Expansion, *Jorunal of Fluids Engineering*, 2002,  
21 124(1): 273-278.
- 22 [44] S.J. Kline, F.A. McClintock, Describing Uncertainties in Single-Sample  
23 Experiments, *Mechanical engineering*, 1953, 75, 3-9
- 24 [45] American Society of Heating, Refrigerating and Air-Conditioning Engineers  
25 (ASHRAE), 2009.
- 26 [46] J. Wu, G. Zhou, M. Wang, A comprehensive assessment of refrigerants for cabin  
27 heating and cooling on electric vehicles, *Applied Thermal Engineering*, 2020, 174,  
28 115258.
- 29 [47] M. A. Bezerra, R. E. Santelli, E. P. Oliveira, L. S. Villar, L. A. Escalera, Response

- 1 surface methodology (RSM) as a tool for optimization in analytical chemistry, *Talanta*,
- 2 2008, 76, Issue 5, 965-977.